Supplement of Atmos. Chem. Phys., 25, 17125–17138, 2025 https://doi.org/10.5194/acp-25-17125-2025-supplement © Author(s) 2025. CC BY 4.0 License.





Supplement of

Atmospheric new particle formation in the eastern region of China: an investigation on mechanism and influencing factors at multiple sites

Jiaqi Jin et al.

Correspondence to: Lin Wang (lin_wang@fudan.edu.cn)

The copyright of individual parts of the supplement might differ from the article licence.

15

20

25

30

35

Text S1. The measurement of chemical species

For the measurement of sulfuric acid (SA) and oxygenated organic molecules (OOMs), a sample flow (8.8 L min⁻¹) was positioned centrally along the axis of the nitrate chemical ionization source, encased by a sheath gas flow (20 L min⁻¹) consisting of high-purity air containing trace gaseous nitric acid to minimize wall loss of analyte molecules. Under the influence of an electric field, nitrate ions were driven toward the center of the sample flow and charged sample molecules. After chemical ionization, approximately 0.8 L min⁻¹ of the ionized sample flow was directed through a 0.3 mm pinhole into three successively evacuated chambers under differential pressure and guided electric fields. [SA] was determined by (Lu et al., 2019):

$$[SA] = C_{SA} \cdot \frac{(HNO_3)_{0-2}SA^- + SA_2^-}{(HNO_3)_{0-2}NO_3^-}$$
 (S1)

where C_{SA} is the calibration coefficient for SA; $(HNO_3)_{0-2}SA^-$, SA_2^- and $(HNO_3)_{0-2}NO_3^-$ represent the signals (cps). The fractional part on the right side represents the normalized signal of SA. [OOMs] was determined by (Kirkby et al., 2016):

$$[00M_{\rm X}] = \frac{C_{\rm SA}}{T_{\rm X}} \cdot \frac{00M_{\rm X} \cdot NO_3^-}{({\rm HNO_3})_{0-2}NO_3^-}$$
 (S2)

where T_X is the mass-to-charge-dependent transmission efficiency relative to SA; $OOM_X \cdot NO_3$ represent the signals (cps).

For the measurement of dimethylamine (DMA) at Wangdu (WD) and Dianshan Lake (DL), the Vocus proton-transfer-reaction time-of-flight mass spectrometer generated protonated water ions through specific voltage (450 V) and current (1.4-1.5 A) settings. The ion source introduced ultra-pure water vapor (20-30 sccm) into focusing ion-molecular reactor (FIMR), where it underwent proton transfer reactions with DMA. Efficient ion-molecule reactions were ensured by a precise control of temperature (100 °C) and pressure (2 mbar). The electric field strength in the FIMR was set to 170 Td, effectively focusing and accelerating the generated ions. The radio frequency amplitude and frequency in big segmented quadrupole were set at 240 V and 2.2×10^6 Hz, respectively. At WD, DMA standard gas was generated by a self-made permeating tube. The permeation rate of the tube was determined by an acid-base calibration. At DL, six species (methyl ethyl ketone, benzene, toluene, m-xylene, 1,3,5-trimethylbezene and α -pinene) were calibrated to obtain the sensitivity for DMA, as the fitting ratio of proton-transfer reaction rate constants to sensitivity of these gases is very close to that of DMA (Wang et al., 2020). The ambient mixing ratio of [DMA] at WD and DL was calculated by (Krechmer et al., 2018):

$$[DMA] = \frac{I}{S_{DMA}}$$
 (S3)

where I is the signal of $C_2H_8N^+$ (cps); S_{DMA} is the sensitivity for DMA.

For the measurement of DMA at Taihu Lake (TL), a pure air flow (1 L min⁻¹) was directed through an ethanol-filled bubbler and subsequently entered a radioactive source to generate protonated ethanol reagent ions. A sample flow (1.35 L min⁻¹) was introduced into the ion-molecule reaction (IMR) chamber, where it mixed with the reagent ion. The pressures in the IMR chamber and the small-segmented quadrupole were maintained at approximately 100 mbar and 2.8 mbar, respectively, to enhance instrument sensitivity. To minimize wall losses, a high sampling flow rate (15 L min⁻¹) was employed, and the sampling line was heated to 50 °C. The calibration method was similar to that at WD. The ambient mixing ratio of [DMA] at TL was calculated by (Yao et al., 2016):

40
$$[DMA] = C_{DMA} \cdot \frac{(DMA)(C_2H_5OH)_{0-1}H^+}{(C_2H_5OH)_{1-3}H^+}$$
 (S4)

where C_{DMA} is the calibration coefficient for DMA. (DMA)(C_2H_5OH)₀₋₁H⁺ and (C_2H_5OH)₁₋₃H⁺ represent the signals (cps).

For the measurement of NH_3 , the sampling process involved drawing ambient air at a flow rate of $0.5 L min^{-1}$ for 60 minutes through a $0.45 \mu m$ filter and into a 10 mL SA absorption solution ($0.01 mol L^{-1}$) held in a porous glass absorber, with a typical sample volume of 30 L. After sampling, the absorption solution was transferred to a 10 mL tube, diluted with water, and then filtered through a $0.22 \mu m$ membrane. The analysis was performed using ion chromatography with a cation exchange column and a conductivity detector. The quantification of $[NH_3]$ was achieved using an external standard method.

Text S2. Data analysis

45

50

55

60

65

70

75

New particle formation (NPF) events were identified based on the characteristics of particle size distributions (PSDs), following two essential criteria: (1) A distinct increase in the number concentration of particles with diameters less than 25 nm need to be observed. The upper size limit of 25 nm is defined, because nucleation events may occur at a certain distance from the observation station in some cases. By the time new particles are detected, their size may have already grown to 25 nm or even larger. (2) Sustained formation and growth of nucleation-mode particles last for at least 1 h accompanied by the characteristic banana-shaped PSD. If the second point is not met, it suggests that the particle formation event is non-regional and may originate from point or line sources of nanoparticles.

Particle formation rate quantifies the growth flux at a specific particle diameter. It was calculated using a balance formula developed by Cai and Jiang (2017), which offers an improved accuracy in estimating coagulation scavenging under conditions of elevated aerosol loading:

$$J_k = \frac{dN_{[d_k, d_u)}}{dt} + \sum_{d_g = d_k}^{d_{u-1}} \sum_{d_i = d_{\min}}^{+\infty} \beta_{(i,g)} N_{[d_i, d_{i+1})} N_{[d_g, d_{g+1})}$$

$$-\frac{1}{2} \sum_{d_g = d_{\min}}^{d_{u-1}} \sum_{d_i^3 = \max(d_{\min}^3, d_k^3 - d_{\min}^3)}^{d_{i+1}^3 + d_{g+1}^3 \le d_u^3} \beta_{(i,g)} N_{[d_i, d_{i+1})} N_{[d_g, d_{g+1})} + n_u GR_u$$
(S5)

where J_k is the formation rate of particles at size d_k (1.4 nm or 1.7 nm in this study); d_u is the calculated upper size bound selected according to different nucleation characteristics; d_{min} is the lower limit of instrument measurement; N is defined as the total number concentration of particles in the corresponding subscript range; β refers to the coagulation coefficient of two particle sizes; n is the particle size distribution function that equals dN/dd_p ; and GR_u is the growth rate of the nearest particle size segment of d_u .

Condensation sink (CS) characterizes the condensing vapor sink caused by pre-existing aerosols and was calculated using the following equation (Kulmala et al., 2013):

$$CS = 2\pi D \sum_{d_{\mathbf{p}}} \beta_{m,d_{\mathbf{p}}} N_{d_{\mathbf{p}}}$$
 (S6)

where D represents the diffusion coefficient of the condensing vapor (SA), and $\beta_{m,dp}$ is the transitional regime correction factor. The coagulation scavenging of particles was estimated through CS:

$$CoagS_{d_p} = CS \left(\frac{d_p}{0.64}\right)^{-1.7}$$
 (S7)

The volatility of OOMs was estimated by the following formula (Mohr et al., 2019):

$$\log_{10} C^* (300 \text{ K}) = (25 - n_C)b_C - (n_O - 3n_N)b_O - \frac{2(n_O - 3n_N)n_C}{n_C + n_O - 3n_N}b_{CO} - n_N b_N$$
 (S8)

where C^* is the saturation mass concentration of the molecule at 300 K, and n_C , n_O and n_N represent molecular number of carbon, oxygen and nitrogen, respectively. $b_C=0.475$; $b_O=0.2$; $b_{CO}=0.9$; $b_N=2.5$. At different ambient temperatures, C^* was estimated by (Donahue et al., 2011):

$$C^*(T) = C^*(300 \text{ K}) \exp\left(\frac{\Delta H_{\text{vap}}}{R} \left(\frac{1}{300 \text{ K}} - \frac{1}{T}\right)\right)$$
 (S9)

where R is the gas constant, T is the temperature in Kelvin, and $\triangle H_{\text{vap}}$ is the vaporization enthalpy, which was calculated by (Epstein et al., 2010):

$$\Delta H_{\text{vap}} = -5.7 \log_{10} C^* (300 \text{ K}) + 129$$
 (S10)

Text S3. Introduction of modules in the cluster dynamics-multicomponent sectional model

80

85

90

95

100

105

110

The cluster dynamics module simulated the evolution of clusters. Clusters with more than five SA or DMA molecules were not included in the simulation. Collision rate coefficients between molecules and clusters were calculated based on kinetic gas theory (Ortega et al., 2012). Temperature modulates nucleation processes by altering the evaporation rates of clusters, which were derived from collision coefficients and the cluster formation free energy referenced from the literature (Olenius et al., 2017). Among these clusters, SA_1DMA_1 exhibits the most pronounced temperature dependence, and its net formation represents the dominant pathway through which temperature modulates nucleation processes. Reported values for the Gibbs free energy of formation (ΔG) of SA_1DMA_1 at 298.15 K range from -11.0 to -15.4 kcal mol⁻¹ (Olenius et al., 2017; Myllys et al., 2019; Ge et al., 2020; Han et al., 2020). Here, it was set to be -13.5 kcal mol⁻¹ at 298.15 K, according to the value from Myllys et al. (2019).

The sectional module simulated particle growth through condensation, evaporation, coagulation and loss. Particles were distributed into discrete size bins in terms of their geometric diameters, ranging from 1.1 nm to 115.9 nm. Each bin was further divided into two parts, which recorded the mass of SA-DMA clusters and OOMs, respectively. Particles in each bin were assumed to be totally mixed with these condensable species, meaning they shared the same chemical composition. Theoretically, this module can simulate the initial growth of newly formed particles, enabling the prediction of $J_{1.7}$. However, the sectional module was limited in some cases, because simulated PSDs might exceed the model boundaries.

The sectional module focused on the formation and growth of newly formed particles, and particles that were obviously not from new particle formation needed to be excluded from the simulation. This was achieved by implementing a time-varying simulation domain, whose bounds were determined for each NPF event by applying a polynomial fit to the observed PSD to identify the size range attributable to NPF. Particles within the domain underwent condensation, evaporation, and coagulation, while particles outside were pre-existing and contribute to the coagulation sink of particles within the domain. This approach not only reduces computational costs, but also focuses on NPF itself rather than the evolution of pre-existing or large primary particles. The model performs well for some NPF events (Fig. S2a). However, in other cases, high OOMs concentrations lead to extremely rapid growth, and particles generated by NPF quickly exceed the boundary of the simulation domain (Fig. S2b). This causes a decrease on the simulated particle number concentration (N) beyond the critical size (k) when calculating particle formation rate in Eq. (S5), resulting in smaller or even negative values. Even without an explicit domain boundary, simulated particles can exceed the intrinsic size limit of the model (Fig. S2c). If OOMs are not treated as condensable vapors and only the effect of SA and its clusters are considered, the simulated particles do not exceed the boundary (Fig. S2d).

Text S4. The derivation of scaled nucleation rate

The scaled process of particle formation rate is similar to that of SA dimer concentration. The scaled $J_{1.4}$ ($J_{1.4,scaled}$) was derived below:

$$J_{1.4,\text{scaled}} = J_{1.4,\text{meas}} \cdot C_{1.4} (CS_{\text{median}}, [DMA]_{\text{med}})$$
(S11)

where $J_{1.4,\text{meas}}$ refers to the measured $J_{1.4}$; $C_{1.4}$ (CS_{median}, [DMA]_{median}) is defined as the scaling coefficient for $J_{1.4,\text{meas}}$, and was calculated by:

$$C_{1.4}(CS_{\text{median}}, [DMA]_{\text{median}}) = \frac{J_{1.4,\text{sim,median}}}{J_{1.4 \text{ sim}}}$$
(S12)

where $J_{1.4,\text{sim}}$ is the simulated $J_{1.4}$, which is calculated by inputting measured data in the model; $J_{1.4,\text{sim},\text{median}}$ is the simulated $J_{1.4}$ with median inputs of CS and DMA concentration ([DMA]), and is calculated by inputting measured SA monomer concentration ([SA₁]) and temperature, but the median [DMA] (2.3 pptv) and the median CS (0.017 s⁻¹) in all NPF events. $J_{1.4,\text{sim},\text{median}}$ can be regarded as the theoretical $J_{1.4,\text{meas}}$ when measured [DMA] and CS reach the median values. A crucial assumption of this scaled method is that $J_{1.4,\text{sim}}$ and $J_{1.4,\text{meas}}$ are approximately equal.

Based on $J_{1.4}$, the scaled $J_{1.7}$ ($J_{1.7,\text{scaled}}$) was derived below:

$$J_{1.7,\text{scaled}} = J_{1.7,\text{meas}} \cdot C_{1.7}(\text{CS}_{\text{median}}, [\text{DMA}]_{\text{median}}, P_{\text{median}})$$

$$= J_{1.7,\text{meas}} \cdot \frac{J_{1.7,\text{sim},\text{median}}}{J_{1.7,\text{sim}}}$$

$$= J_{1.7,\text{meas}} \cdot \frac{J_{1.4,\text{sim},\text{median}} \cdot P_{\text{median}}}{J_{1.4,\text{sim}} \cdot P}$$
(S13)

where $J_{1.7,\text{meas}}$ is the measured $J_{1.7}$; $C_{1.7}$ (CS_{median}, [DMA]_{median}, P_{median}) is the scaling coefficient for $J_{1.7,\text{meas}}$; $J_{1.7,\text{sim}}$ is the simulated $J_{1.7,\text{sim}}$; $J_{1.7,\text{sim},\text{median}}$ is the simulated $J_{1.7}$ with median measured inputs, except for [SA₁] and temperature; P is the survival probability from 1.4 nm to 1.7 nm calculated by Eq. (1); P_{median} is the median P (0.67) in all NPF events.

Text S5. The simulation of $J_{1.4}$

120

125

130

135

140

145

150

155

There is an acceptable consistency between $J_{1.4,\text{meas}}$ and $J_{1.4,\text{sim}}$ when observational and model uncertainties are considered (Fig. S7). Deviations reported in previous laboratory or field studies were typically within 1 order of magnitude (Kürten et al., 2018; Cai et al., 2021; Xiao et al., 2021), smaller than those in our study. This discrepancy likely arises from differences in uncertainty ranges. For a single observation, the measurement uncertainty is relatively low (Freshour et al., 2014), and the resulting simulation uncertainty can be controlled within a narrow range. However, our measurement spanned several years and involved multiple sites, may amplifying the overall uncertainty in $J_{1.4}$.

The uncertainty range of $J_{1.4,sim}$ need to be analyzed basically. Overall, the output range spans approximately 3 orders of magnitude, indicating high model sensitivity to input parameters. Theoretically, particle formation rate is approximately proportional to $[SA_1]^4$ in SA-DMA nucleation, and this relationship is particularly evident under high CS and high [DMA] (Cai et al., 2021). In actual observations, the measured data (Fig. 1) did not fully conform to this functional relationship. which might arise from other influencing factors. For example, the substantial temperature variations likely accounted for the large fluctuations in particle formation rate observed at a given $[SA_1]$ (Fig. 6). If data points at TL (high temperature) are removed in Fig. 6, it is not difficult to find that the rest of data points generally follow the functional relationship. Considering the uncertainty of $[SA_1]$ merely (+100%/-50%, Table S1), the propagated uncertainty of $J_{1.4,sim}$ is estimated to be +1600%/-94%. Since there is no simple algebraic relation between [DMA] and $J_{1.4}$, their quantitative dependence need be inferred empirically. An urban study reflected that $J_{1.4}$ roughly varied in proportion to twice of the change of [DMA] (1-5 pptv) accounting for other influencing factors (Cai et al., 2021). Considering the uncertainty of [DMA] (+150%/-60%) merely, the uncertainty of other influencing factors (Cai et al., 2021). In short, by superimposing the uncertainty of input values, the overall uncertainty in modeled $J_{1.4}$, resulting from the propagation of measured precursor uncertainties, is quantitatively reasonable.

Text S6. The effect of temperature on $J_{1.7}$

Similar to $J_{1.4,\text{scaled}}$ (Fig. 6), $J_{1.7,\text{scaled}}$ also exhibits strong temperature dependence (Fig. S9). After incorporating the contribution of OOMs to the growth rate of 1.4-1.7 nm particles ($GR_{1.4-1.7}$), $J_{1.7,\text{sim}}$ improves significantly, reaching a level comparable to $J_{1.4,\text{sim}}$ (Fig. S7). The survival probability (P) mainly depends on $GR_{1.4-1.7}$ and CS, and is not directly related to temperature. It is notice that temperature indirectly influences $GR_{1.4-1.7}$ through three pathways. The first path is the effect on condensation process, including collision rate between molecules and particles and Kelvin effect (Tröstl et al., 2016), which are minor and are considered by Eq. (2). The second is the effect on the volatility of individual OOMs species (Epstein et al., 2010), corrected using Eq. (S10). The third is the effect on organic oxidation rates, which alter the number of effective oxygen of OOMs to change their volatilities. This path involves the whole system of organic oxidation in the atmosphere and is beyond the scope of this study. The third effect has been identified to be weaker than the second one in a chamber investigation (Caudillo et al., 2021), and can be relatively neglected to some extent.

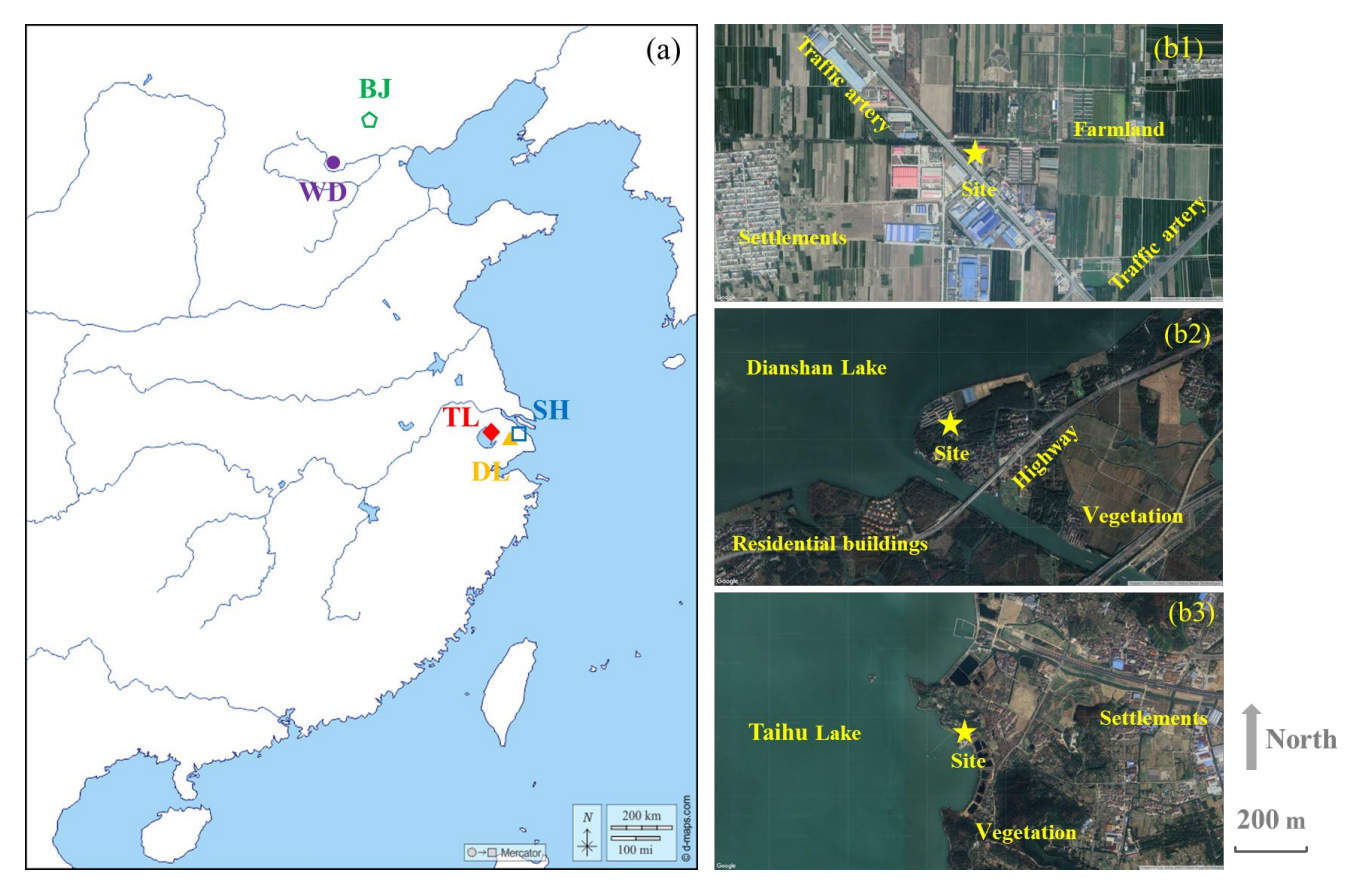


Figure S1: The location of the measurement sites: (a) The overall distribution in the eastern region of China (© d-maps 2025); (b1) WD (© Google Maps 2025); (b2) DL (© Google Maps 2025); (b3) TL (© Google Maps 2025). The location of Beijing site (BJ) and Shanghai site (SH) was introduced in the corresponding studies (Yao et al., 2018; Cai et al., 2021).

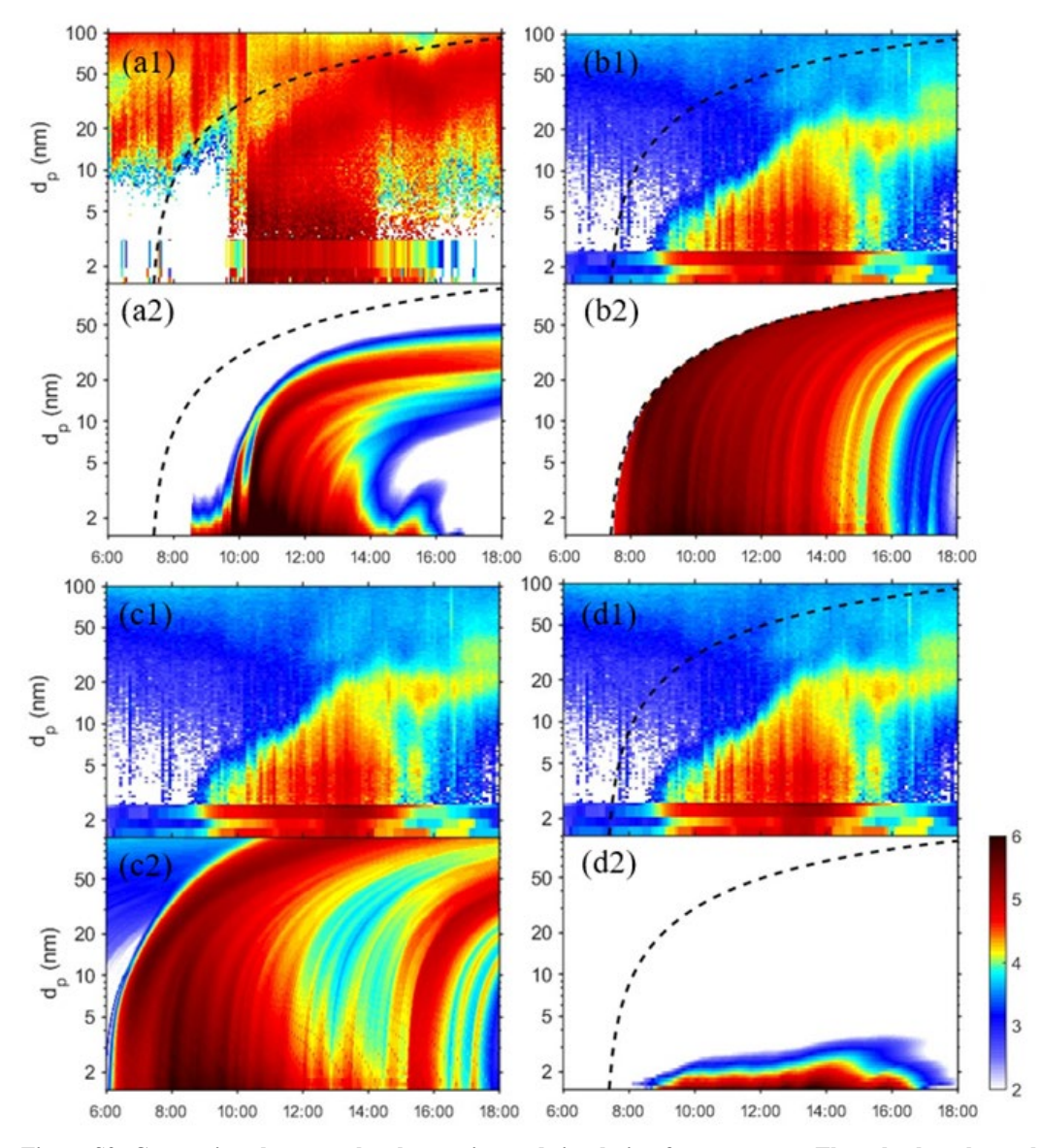


Figure S2: Comparison between the observation and simulation for two events. The color bar shows the \log_{10} values of the particle size distribution ($dN = d\log_{10} dp$ in units of cm⁻³) (a) The NPF events on January 20th, 2019 at WD, consists of (a1) the observed PSD and (a2) the simulated PSD considering both OOMs and the domain boundary. (b)-(d) The NPF events on January 27th, 2023 at DL. The observed PSDs are the same in (b1), (c1) and (d1). The simulated PSDs in (b)-(d) have different simulation settings: (b2) with OOMs and the domain boundary; (c2) with OOMs but without the domain boundary; (c2) without OOMs but with the domain boundary. The dashed curves are the upper boundary of the simulation domain for NPF.

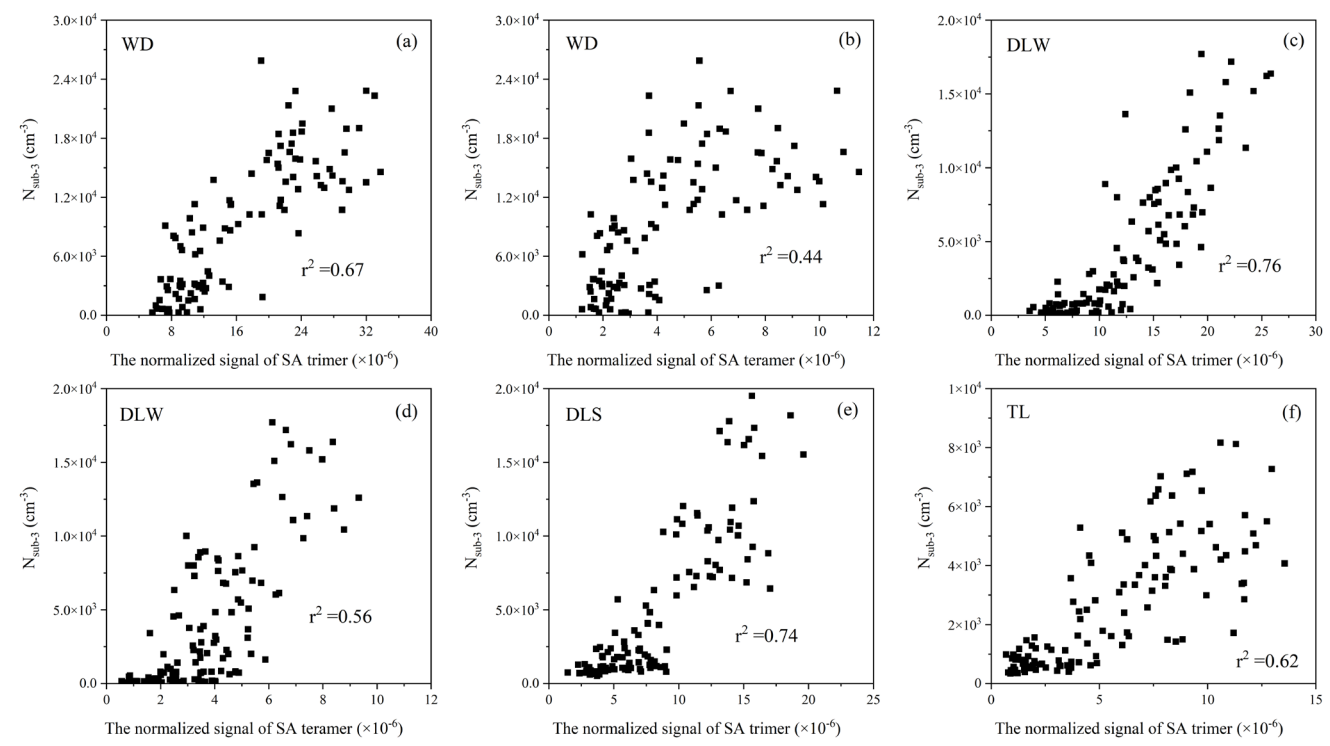


Figure S3: The correlation between the normalized signal of SA clusters and the number concentration of particles below 3 nm (N_{sub-3}): (a)-(b) January 20th, 2019 at WD; (c)-(d) January 27th, 2023 at DL in winter (DLW); (e) May 2nd, 2023 at DL in spring (DLS); (f) August 7th, 2023 at TL. Only data recorded in the daytime (06:00-18:00 TL) were included in the analysis.

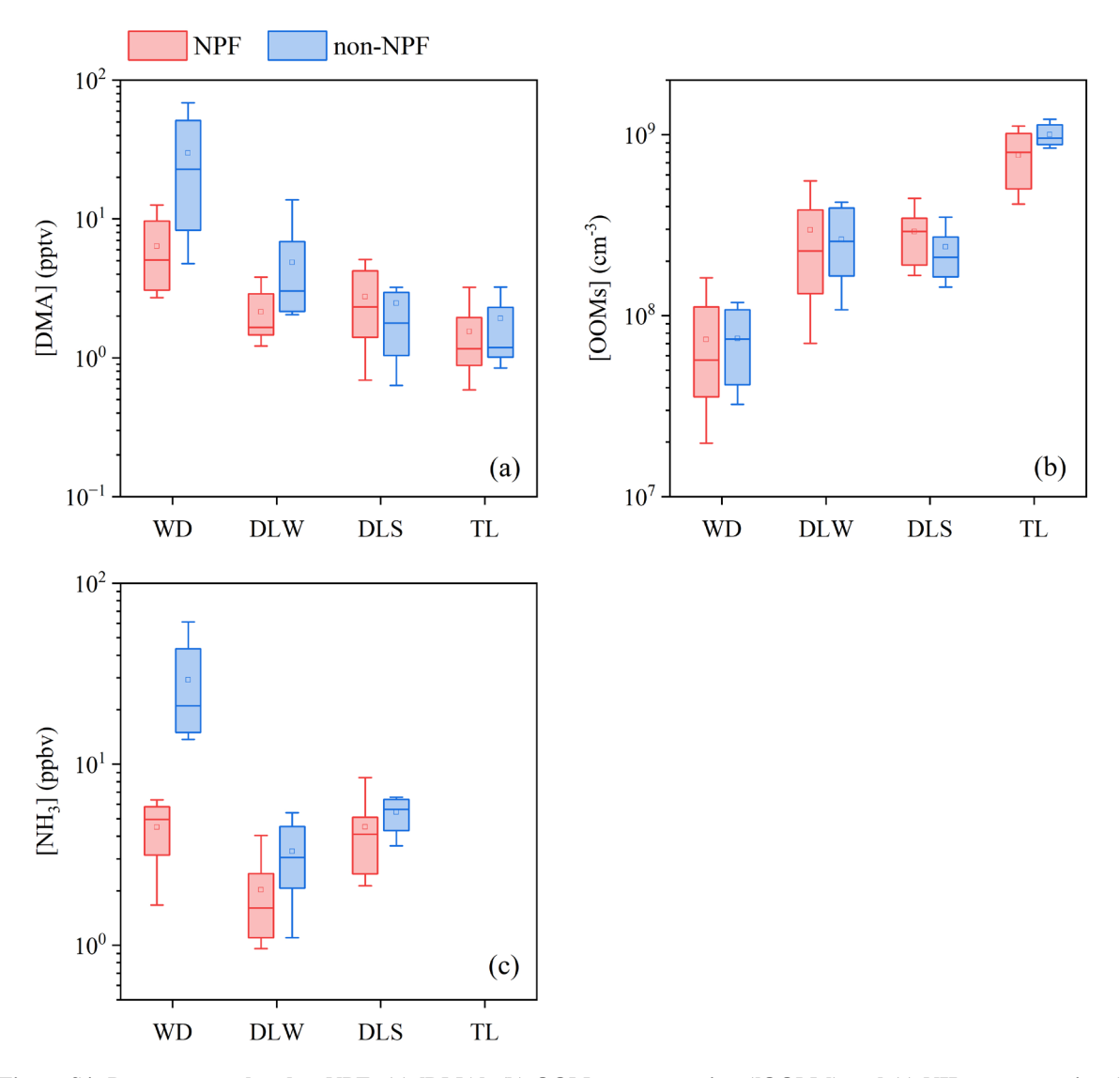


Figure S4: Parameters related to NPF: (a) [DMA], (b) OOMs concentration ([OOMs]) and (c) NH₃ concentration ([NH₃]) during NPF periods and non-NPF periods. The NPF period is defined as the period with the maximum value of $J_{1.7}$ in each NPF event, and the non-NPF period is defined as the median range of all NPF periods (9:00-11:00 TL) in non-NPF days. In order to eliminate the influence of precipitation, only sunny and cloudy days are selected for non-NPF. The transverse lines and square markers inside the boxes indicate mean values and median values, respectively. The bottom and top edges of the box indicate the 25th and 75th percentiles, respectively. The bottom and top edges of the boxes indicate the 10th and 90th percentiles, respectively.

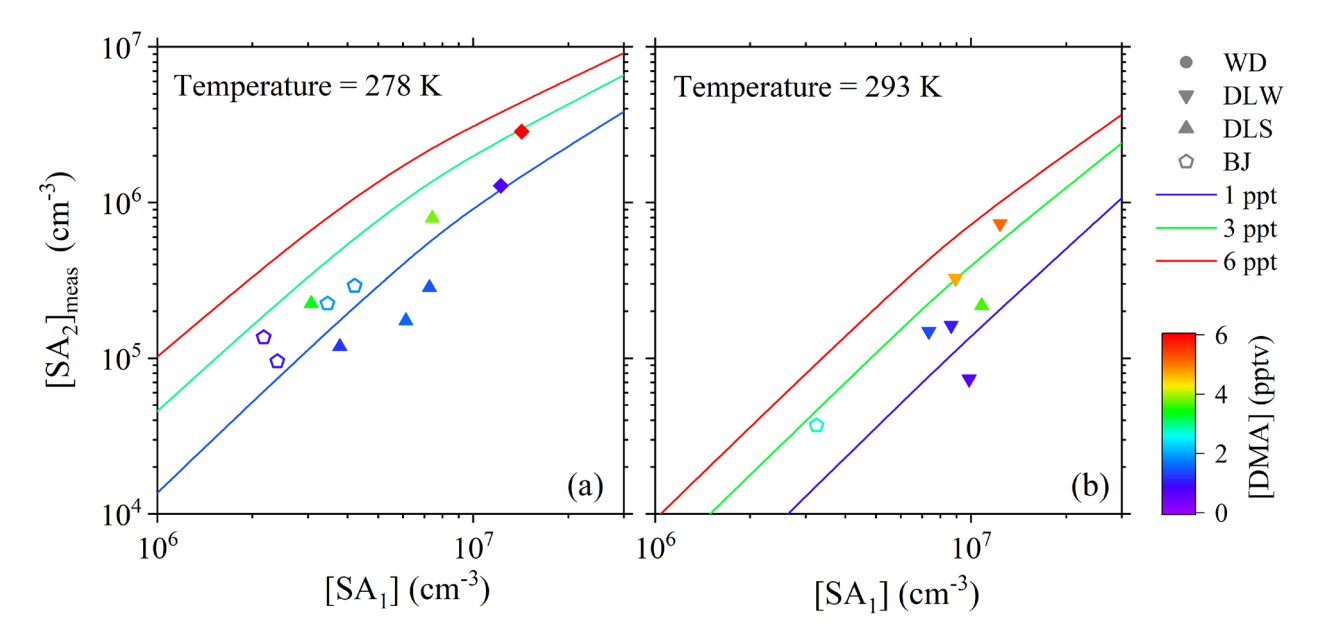


Figure S5: $[SA_2]_{meas}$ as a function of $[SA_1]$ under a [DMA] gradient in two temperature ranges, 278 ± 3 K and 293 ± 3 K. Each temperature rang is indicated by its median value. The simulated lines are calculated by the discrete-sectional model the median value of the temperature range, i.e., 278 K or 293 K. CS for the simulated lines is its median value (0.017 s^{-1}) in all NPF events.

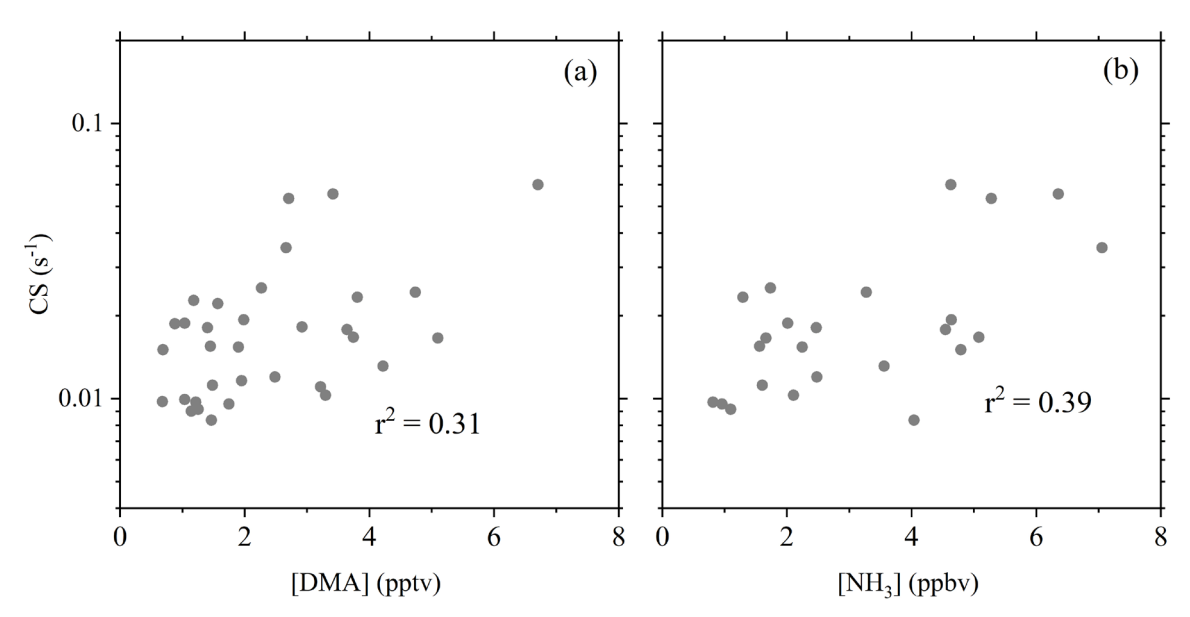


Figure S6: Correlations between the concentrations of basic precursors and CS during NPF periods: (a) [DMA] at WD, DL and TL; (b) [NH₃] at WD and DL. The NPF period is defined as the period with the maximum value of $J_{1.7}$ in each NPF event.

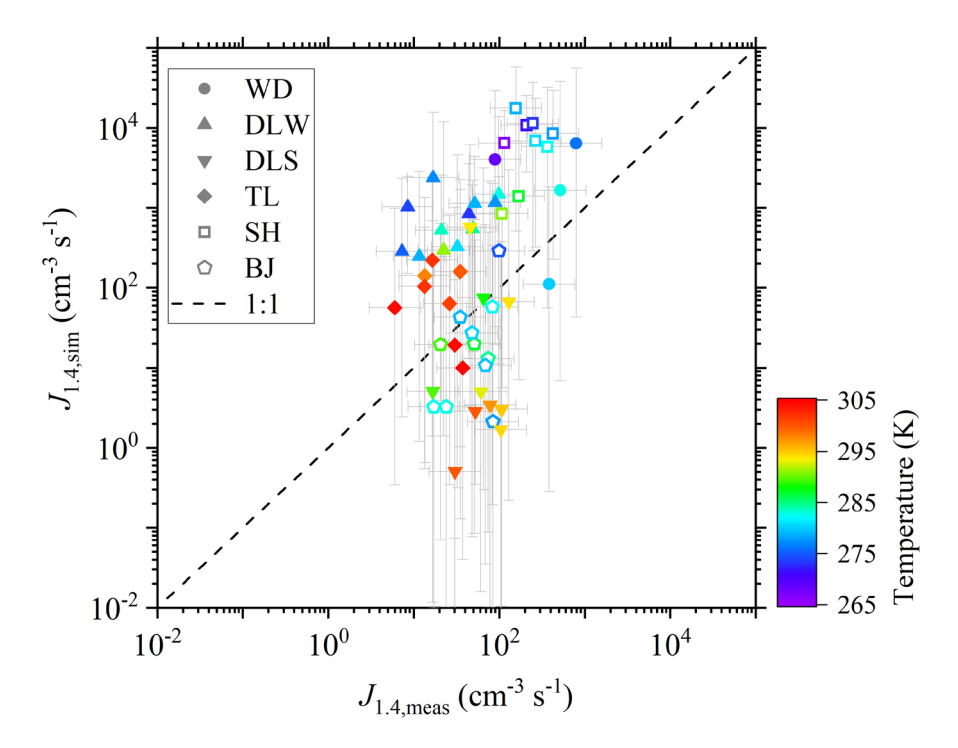


Figure S7: The comparison between $J_{1.4,meas}$ and $J_{1.4,sim}$. Horizontal and vertical error bars connected with each symbol indicate the uncertainties of x-axis and y-axis, respectively.

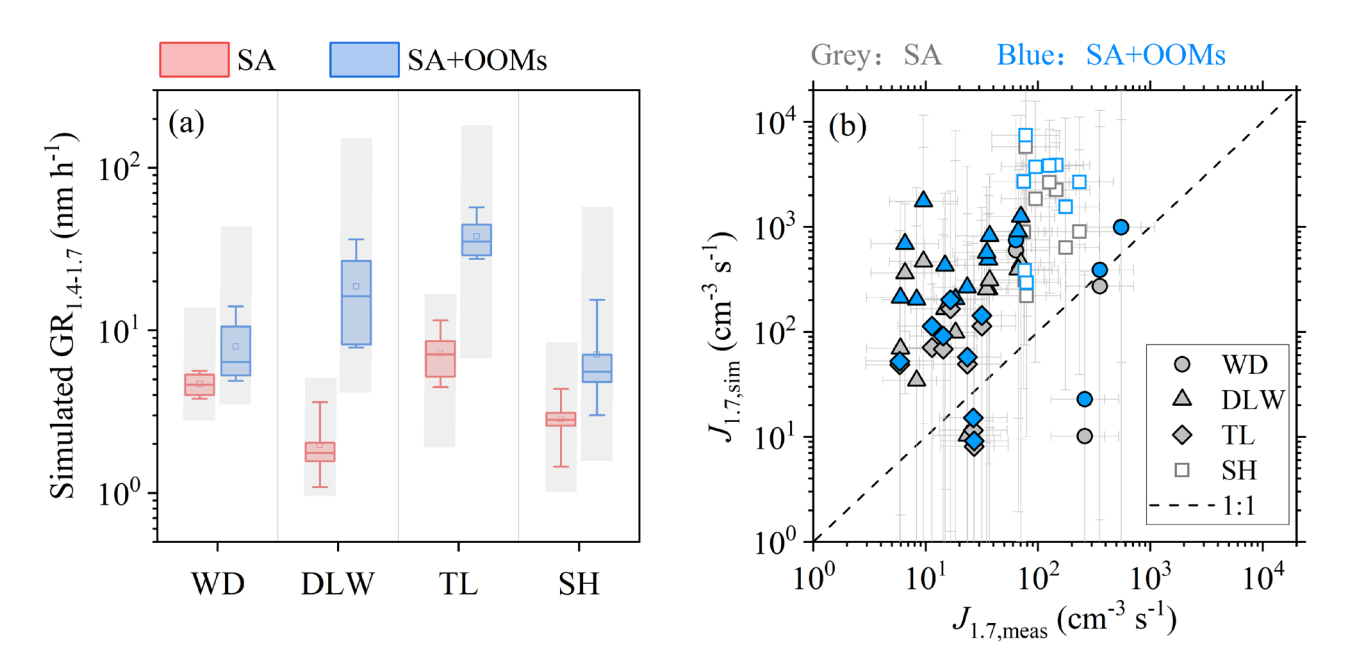


Figure S8: The simulation of GR_{1.4-1.7} and $J_{1.7}$. (a) The comparison of simulated GR_{1.4-1.7} contributed by SA and its clusters (i.e. SA in the legend), as well as SA and its clusters plus OOMs in different campaigns. The transverse lines and square markers inside the boxes indicate mean values and median values, respectively. The bottom and top edges of the box indicate the 25th and 75th percentiles, respectively. The bottom and top edges of the whisker lines outside of the boxes indicate the 10th and 90th percentiles, respectively. The shade boxes indicate the ranges of uncertainties. (b) The comparison between $J_{1.7,\text{meas}}$ and $J_{1.7,\text{sim}}$. Horizontal and vertical error bars connected with each symbol indicate the uncertainties of x-axis and y-axis, respectively.

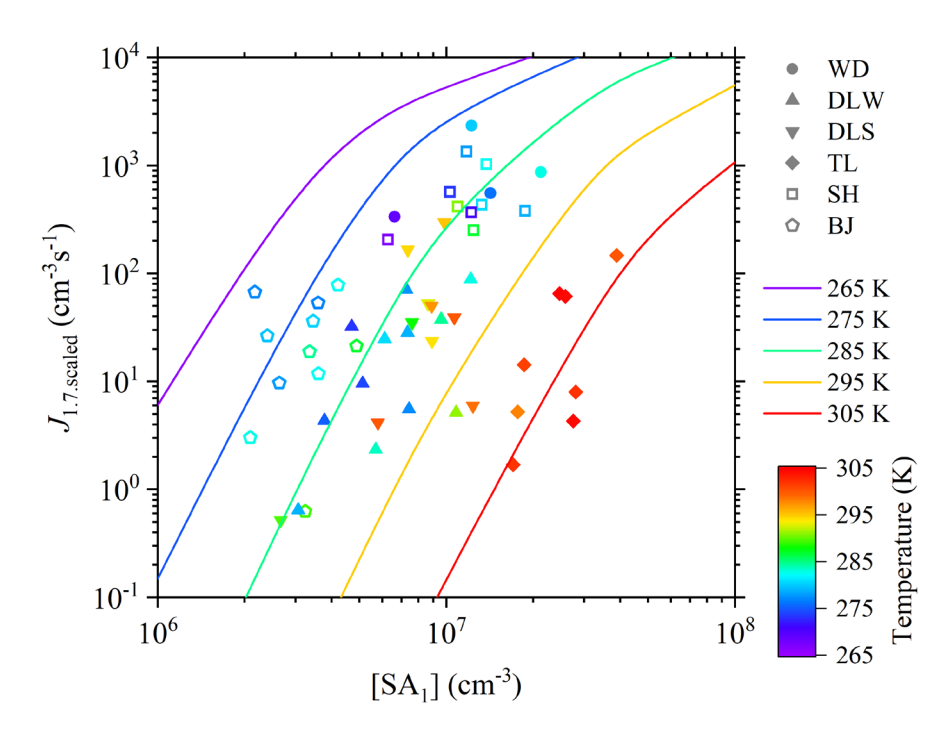


Figure S9: $J_{1.7,\text{scaled}}$ as a function of [SA₁] under the temperature gradient. Each symbol indicates one NPF event with a time resolution of 30 min, which was selected when $J_{1.7,\text{meas}}$ reaches maximum. [DMA], CS and P for the simulated lines by the discrete-sectional model are their median values in all NPF events, i.e., 0.017 s⁻¹, 2.3 pptv and 0.67, respectively. To visualize the effect of temperature, the color of the simulated lines corresponds to the color bar.

Table S1: The range of uncertainty associated with parameters in models.

| Input | [SA] | [DMA] | [OOMs] | CS | Particle formation rate |
|-------------|------------|------------|---------------------------------|------|-------------------------|
| Uncertainty | +100%/-50% | +150%/-60% | $+200\%/-66\%$ $(\log C*\pm 1)$ | ±10% | +100%/-50% |

References

210

Cai, R. and Jiang, J.: A new balance formula to estimate new particle formation rate: reevaluating the effect of coagulation scavenging, Atmos. Chem. Phys., 17, 12659–12675, https://doi.org/10.5194/acp-17-12659-2017, 2017.

Cai, R., Yan, C., Yang, D., Yin, R., Lu, Y., Deng, C., Fu, Y., Ruan, J., Li, X., Kontkanen, J., Zhang, Q., Kangasluoma, J., Ma, Y., Hao, J., Worsnop, D. R., Bianchi, F., Paasonen, P., Kerminen, V.-M., Liu, Y., Wang, L., Zheng, J., Kulmala, M., and Jiang, J.: Sulfuric acid-amine nucleation in urban Beijing, Atmos. Chem. Phys., 21, 2457–2468, https://doi.org/10.5194/acp-21-2457-2021, 2021.

Caudillo, L., Rorup, B., Heinritzi, M., Marie, G., Simon, M., Wagner, A. C., Mueller, T., Granzin, M., Amorim, A., Ataei, F.,
Baalbaki, R., Bertozzi, B., Brasseur, Z., Chiu, R., Chu, B., Dada, L., Duplissy, J., Finkenzeller, H., Carracedo, L. G., He, X.-C., Hofbauer, V., Kong, W., Lamkaddam, H., Lee, C. P., Lopez, B., Mahfouz, N. G. A., Makhmutov, V., Manninen, H. E., Marten, R., Massabò, D., Mauldin, R. L., Mentler, B., Molteni, U., Onnela, A., Pfeifer, J., Philippov, M., Piedehierro, A. A., Schervish, M., Scholz, W., Schulze, B., Shen, J., Stolzenburg, D., Stozhkov, Y., Surdu, M., Tauber, C., Tham, Y. J., Tian, P., Tomé, A., Vogt, S., Wang, M., Wang, D. S., Weber, S. K., Welti, A., Wang, Y., Wu, Y., Zauner-Wieczorek, M., Baltensperger,
U., El Haddad, I., Flagan, R. C., Hansel, A., Höhler, K., Kirkby, J., Kulmala, M., Lehtipalo, K., Moehler, O., Saathoff, H., Volkamer, R., Winkler, P. M., Donahue, N. M., Kuerten, A., and Curtius, J.: Chemical composition of nanoparticles from α-pinene nucleation and the influence of isoprene and relative humidity at low temperature, Atmos. Chem. Phys., 21, 17099–17114, https://doi.org/10.5194/acp-21-17099-2021, 2021.

Donahue, N. M., Epstein, S. A., Pandis, S. N., and Robinson, A. L.: A two-dimensional volatility basis set: 1. organic-aerosol

- mixing thermodynamics, Atmos. Chem. Phys., 11, 3303–3318, https://doi.org/10.5194/acp-11-3303-2011, 2011. Epstein, S. A., Riipinen, I., and Donahue, N. M.: A semiempirical correlation between enthalpy of vaporization and saturation concentration for organic aerosol, Environ. Sci. Technol., 44, 743–748, https://doi.org/10.1021/es902497z, 2010.
 - Freshour, N. A., Carlson, K. K., Melka, Y. A., Hinz, S., Panta, B., and Hanson, D. R.: Amine permeation sources characterized with acid neutralization and sensitivities of an amine mass spectrometer, Atmos. Meas. Tech., 7, 3611–3621,
- 235 https://doi.org/10.5194/amt-7-3611-2014, 2014.
 - Ge, P., Luo, G., Huang, W., Xie, H., Chen, J., and Luo, Y.: Theoretical study of the hydration effects on alkylamine and alkanolamine clusters and the atmospheric implication, Chemosphere, 243, 125323, https://doi.org/10.1016/j.chemosphere.2019.125323, 2020.
 - Han, J., Wang, L., Zhang, H., Su, Q., Zhou, X., and Liu, S.: Determinant factor for thermodynamic stability of sulfuric acid-amine complexes, J. Phys. Chem. A, 124, 10246–10257, https://doi.org/10.1021/acs.jpca.0c07908, 2020.
- amine complexes, J. Phys. Chem. A, 124, 10246–10257, https://doi.org/10.1021/acs.jpca.0c07908, 2020.
 Kirkby, J., Duplissy, J., Sengupta, K., Frege, C., Gordon, H., Williamson, C., Heinritzi, M., Simon, M., Yan, C., Almeida, J., Tröstl, J., Nieminen, T., Ortega, I. K., Wagner, R., Adamov, A., Amorim, A., Bernhammer, A.-K., Bianchi, F., Breitenlechner, M., Brilke, S., Chen, X., Craven, J., Dias, A., Ehrhart, S., Flagan, R. C., Franchin, A., Fuchs, C., Guida, R., Hakala, J., Hoyle, C. R., Jokinen, T., Junninen, H., Kangasluoma, J., Kim, J., Krapf, M., Kürten, A., Laaksonen, A., Lehtipalo, K., Makhmutov,
- V., Mathot, S., Molteni, U., Onnela, A., Peräkylä, O., Piel, F., Petäjä, T., Praplan, A. P., Pringle, K., Rap, A., Richards, N. A. D., Riipinen, I., Rissanen, M. P., Rondo, L., Sarnela, N., Schobesberger, S., Scott, C. E., Seinfeld, J. H., Sipilä, M., Steiner, G., Stozhkov, Y., Stratmann, F., Tomé, A., Virtanen, A., Vogel, A. L., Wagner, A. C., Wagner, P. E., Weingartner, E., Wimmer, D., Winkler, P. M., Ye, P., Zhang, X., Hansel, A., Dommen, J., Donahue, N. M., Worsnop, D. R., Baltensperger, U., Kulmala, M., Carslaw, K. S., and Curtius, J.: Ion-induced nucleation of pure biogenic particles, Nature, 533, 521-526,
- https://doi.org/10.1038/nature17953, 2016.
 Krechmer, J., Lopez-Hilfiker, F., Koss, A., Hutterli, M., Stoermer, C., Deming, B., Kimmel, J., Warneke, C., Holzinger, R., Jayne, J., Worsnop, D., Fuhrer, K., Gonin, M., and de Gouw, J.: Evaluation of a new reagent-ion source and focusing ion—molecule reactor for use in proton-transfer-reaction mass spectrometry, Anal. Chem., 90, 12011–12018, https://doi.org/10.1021/acs.analchem.8b02641, 2018.
- Kulmala, M., Kontkanen, J., Junninen, H., Lehtipalo, K., Manninen, H. E., Nieminen, T., Petäjä, T., Sipilä, M., Schobesberger, S., Rantala, P., Franchin, A., Jokinen, T., Järvinen, E., Äijälä, M., Kangasluoma, J., Hakala, J., Aalto, P. P., Paasonen, P., Mikkilä, J., Vanhanen, J., Aalto, J., Hakola, H., Makkonen, U., Ruuskanen, T., Mauldin, R. L., Duplissy, J., Vehkamäki, H., Bäck, J., Kortelainen, A., Riipinen, I., Kurtén, T., Johnston, M. V., Smith, J. N., Ehn, M., Mentel, T. F., Lehtinen, K. E. J., Laaksonen, A., Kerminen, V.-M., and Worsnop, D. R.: Direct observations of atmospheric aerosol nucleation, Science, 339, 943–946,
- https://doi.org/10.1126/science.1227385, 2013.
 Kürten, A., Li, C., Bianchi, F., Curtius, J., Dias, A., Donahue, N. M., Duplissy, J., Flagan, R. C., Hakala, J., Jokinen, T., Kirkby, J., Kulmala, M., Laaksonen, A., Lehtipalo, K., Makhmutov, V., Onnela, A., Rissanen, M. P., Simon, M., Sipilä, M., Stozhkov, Y., Tröstl, J., Ye, P., and McMurry, P. H.: New particle formation in the sulfuric acid—dimethylamine—water system: reevaluation of CLOUD chamber measurements and comparison to an aerosol nucleation and growth model, Atmos. Chem.
- Phys., 18, 845–863, https://doi.org/10.5194/acp-18-845-2018, 2018.
 Lu, Y., Yan, C., Fu, Y., Chen, Y., Liu, Y., Yang, G., Wang, Y., Bianchi, F., Chu, B., Zhou, Y., Yin, R., Baalbaki, R., Garmash, O., Deng, C., Wang, W., Liu, Y., Petäjä, T., Kerminen, V.-M., Jiang, J., Kulmala, M., and Wang, L.: A proxy for atmospheric daytime gaseous sulfuric acid concentration in urban Beijing, Atmos. Chem. Phys., 19, 1971–1983, https://doi.org/10.5194/acp-19-1971-2019, 2019.
- Mohr, C., Thornton, J. A., Heitto, A., Lopez-Hilfiker, F. D., Lutz, A., Riipinen, I., Hong, J., Donahue, N. M., Hallquist, M., Petäjä, T., Kulmala, M., and Yli-Juuti, T.: Molecular identification of organic vapors driving atmospheric nanoparticle growth, Nat. Commun., 10, 4442, https://doi.org/10.1038/s41467-019-12473-2, 2019.
 - Myllys, N., Kubečka, J., Besel, V., Alfaouri, D., Olenius, T., Smith, J. N., and Passananti, M.: Role of base strength, cluster structure and charge in sulfuric-acid-driven particle formation, Atmos. Chem. Phys., 19, 9753–9768,
- https://doi.org/10.5194/acp-19-9753-2019, 2019.
 Olenius, T., Halonen, R., Kurtén, T., Henschel, H., Kupiainen-Määttä, O., Ortega, I. K., Jen, C. N., Vehkamäki, H., and Riipinen,

- I.: New particle formation from sulfuric acid and amines: Comparison of monomethylamine, dimethylamine, and trimethylamine, J. Geophys. Res.-Atmos., 122, 7103–7118, https://doi.org/10.1002/2017JD026501, 2017.
- Ortega, I. K., Kupiainen, O., Kurtén, T., Olenius, T., Wilkman, O., McGrath, M. J., Loukonen, V., and Vehkamäki, H.: From quantum chemical formation free energies to evaporation rates, Atmos. Chem. Phys., 12, 225–235, https://doi.org/10.5194/acp-12-225-2012, 2012.
 - Tröstl, J., Chuang, W. K., Gordon, H., Heinritzi, M., Yan, C., Molteni, U., Ahlm, L., Frege, C., Bianchi, F., Wagner, R., Simon, M., Lehtipalo, K., Williamson, C., Craven, J. S., Duplissy, J., Adamov, A., Almeida, J., Bernhammer, A.-K., Breitenlechner, M., Brilke, S., Dias, A., Ehrhart, S., Flagan, R. C., Franchin, A., Fuchs, C., Guida, R., Gysel, M., Hansel, A., Hoyle, C. R.,
- Jokinen, T., Junninen, H., Kangasluoma, J., Keskinen, H., Kim, J., Krapf, M., Kürten, A., Laaksonen, A., Lawler, M., Leiminger, M., Mathot, S., Möhler, O., Nieminen, T., Onnela, A., Petäjä, T., Piel, F. M., Miettinen, P., Rissanen, M. P., Rondo, L., Sarnela, N., Schobesberger, S., Sengupta, K., Sipilä, M., Smith, J. N., Steiner, G., Tomè, A., Virtanen, A., Wagner, A. C., Weingartner, E., Wimmer, D., Winkler, P. M., Ye, P., Carslaw, K. S., Curtius, J., Dommen, J., Kirkby, J., Kulmala, M., Riipinen, I., Worsnop, D. R., Donahue, N. M., and Baltensperger, U.: The role of low-volatility organic compounds in initial particle growth in the atmosphere, Nature, 533, 527–531, https://doi.org/10.1038/nature18271, 2016.
- Wang, Y., Yang, G., Lu, Y., Liu, Y., Chen, J., and Wang, L.: Detection of gaseous dimethylamine using vocus proton-transfer-reaction time-of-flight mass spectrometry, Atmos. Environ., 243, 117875, https://doi.org/10.1016/j.atmosenv.2020.117875, 2020.
- Xiao, M., Hoyle, C. R., Dada, L., Stolzenburg, D., Kuerten, A., Wang, M., Lamkaddam, H., Garmash, O., Mentler, B., Molteni,
 U., Baccarini, A., Simon, M., He, X.-C., Lehtipalo, K., Ahonen, L. R., Baalbaki, R., Bauer, P. S., Beck, L., Bell, D., Bianchi,
 F., Brilke, S., Chen, D., Chiu, R., Dias, A., Duplissy, J., Finkenzeller, H., Gordon, H., Hofbauer, V., Kim, C., Koenig, T. K.,
 Lampilahti, J., Lee, C. P., Li, Z., Mai, H., Makhmutov, V., Manninen, H. E., Marten, R., Mathot, S., Mauldin, R. L., Nie, W.,
 Onnela, A., Partoll, E., Petäjä, T., Pfeifer, J., Pospisilova, V., Quéléver, L. L. J., Rissanen, M., Schobesberger, S., Schuchmann,
 S., Stozhkov, Y., Tauber, C., Tham, Y. J., Tomé, A., Vazquez-Pufleau, M., Wagner, A. C., Wagner, R., Wang, Y., Weitz, L.,
- Wimmer, D., Wu, Y., Yan, C., Ye, P., Ye, Q., Zha, Q., Zhou, X., Amorim, A., Carslaw, K., Curtius, J., Hansel, A., Volkamer, R., Winkler, P. M., Flagan, R. C., Kulmala, M., Worsnop, D. R., Kirkby, J., Donahue, N. M., Baltensperger, U., El Haddad, I., and Dommen, J.: The driving factors of new particle formation and growth in the polluted boundary layer, Atmos. Chem. Phys., 21, 14275–14291, https://doi.org/10.5194/acp-21-14275-2021, 2021.
- Yao, L., Wang, M.-Y., Wang, X.-K., Liu, Y.-J., Chen, H.-F., Zheng, J., Nie, W., Ding, A.-J., Geng, F.-H., Wang, D.-F., Chen, J.-M., Worsnop, D. R., and Wang, L.: Detection of atmospheric gaseous amines and amides by a high-resolution time-of-flight chemical ionization mass spectrometer with protonated ethanol reagent ions, Atmos. Chem. Phys., 16, 14527–14543, https://doi.org/10.5194/acp-16-14527-2016, 2016.
 - Yao, L., Garmash, O., Bianchi, F., Zheng, J., Yan, C., Kontkanen, J., Junninen, H., Mazon, S. B., Ehn, M., Paasonen, P., Sipilä, M., Wang, M., Wang, X., Xiao, S., Chen, H., Lu, Y., Zhang, B., Wang, D., Fu, Q., Geng, F., Li, L., Wang, H., Qiao, L., Yang,
- X., Chen, J., Kerminen, V.-M., Petäjä, T., Worsnop, D. R., Kulmala, M., and Wang, L.: Atmospheric new particle formation from sulfuric acid and amines in a Chinese megacity, Science, 361, 278–281, https://doi.org/10.1126/science.aao4839, 2018.